JACS
JOURNAL OF THE AMERICAN CHEMICAL SOCIETY
Article
pubs.acs.org/JACS

Self-Assembled Microdisk Lasers of Perylenediimides

Zhenyi Yu,[†,‡] Yishi Wu,[*,†] Qing Liao,[§] Haihua Zhang,[§] Shuming Bai,[§] Hui Li,[§] Zhenzhen Xu,[§] Chunlin Sun,[†] Xuedong Wang,[†,‡] Jiannian Yao,[†,∥] and Hongbing Fu[*,†,§,∥]

[†]Beijing National Laboratory for Molecular Sciences (BNLMS), Institute of Chemistry, Chinese Academy of Sciences, Beijing 100190, People's Republic of China

[‡]Graduate University of Chinese Academy of Sciences, Beijing 100049, People's Republic of China

[§]Beijing Key Laboratory for Optical Materials and Photonic Devices (BKLOMPD), Department of Chemistry, Capital Normal University, Beijing 100048, People's Republic of China

[∥]Collaborative Innovation Center of Chemical Science and Engineering, Tianjin 300072, People's Republic of China

Supporting Information

ABSTRACT: Organic solid-state lasers (OSSLs) have been a topic of intensive investigations. Perylenediimide (PDI) derivatives are widely used in organic thin-film transistors and solar cells. However, OSSLs based on neat PDIs have not been achieved yet, owing to the formation of H-aggregates and excimer trap-states. Here, we demonstrated the first PDI-based OSSL from whispering-gallery mode (WGM) hexagonal microdisk (hMD) microcavity of N,N′-bis(1-ethylpropyl)-2,5,8,11-tetrakis(*p*-methyl-phenyl)-perylenediimide (*mp*-PDI) self-assembled from solution. Single-crystal data reveal that *mp*-PDI molecules stack into a loosely packed twisted brickstone arrangement, resulting in J-type aggregates that exhibit a solid-state photoluminescence (PL) efficiency φ > 15%. Moreover, we found that exciton-vibration coupling in J-aggregates leads to an exceptional ultrafast radiative decay, which reduces the exciton diffusion length, in turn, suppresses bimolecular exciton annihilation (bmEA) process. These spectral features, plus the optical feedback provided by WGM-hMD microcavity, enable the observation of multimode lasing as evidenced by nonlinear output, spectral narrowing, and temporal coherence of laser emission. With consideration of high carrier-mobility associated with PDIs, hMDs of *mp*-PDI are attractive candidates on the way to achieve electrically driven OSSL.

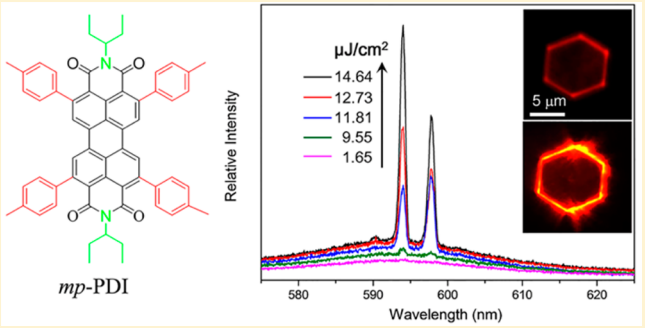

INTRODUCTION

Organic solid-state lasers (OSSLs) have been widely investigated during the past decades,[1] owing to their amenability to low-cost and low-temperature processing,[2] compatibility with plastic substrates,[3] and broad spectral tunability.[4] A variety of optical resonators have been applied for optically pumped OSSLs,[1a] including planar waveguide Fabry-Pérot (FP) microcavity,[5] distributed feedback (DFB),[6] whispering-gallery mode (WGM) microring microresonator,[7] and photonic band gap structures.[8] In these devices, the gain medium generally composed of a polycrystalline thin-film of either polymer or small molecule semiconductors. OSSLs have already been demonstrated in three primary colors of blue, green, and red, which are essential for realization of full-color laser displays.[9] Nevertheless, electrically driven OSSLs remain still a great challenge hindered mainly by two stumbling blocks.[10] (i) The conflicting requirement between large stimulated emission and high charge carrier mobility narrows the range of organic semiconductor gain materials available for electrically driven OSSLs. This is because most organic semiconductors, which exhibit high carrier mobilities, such as pentacene and rubrene, are poorly emissive in the solid state due to serious concentration quenching effect.[11] (ii) Under intense optical or electrical excitation, high density Frenkel excitons will accumulate in the excited state and overlap with each other,and thus, bimolecular exciton−exciton annihilation (bmEA) takes place.[1a,12] As the bmEA process can cause very serious efficiency roll-off at high carrier density in OLED,[12] it is considered as one of the major blocks on the way to achieve electrically pumped OSSLs, in addition to other problematic processes, such as triplet absorption, triplet−triplet annihilation, polaron absorption or annihilation, and so on.[12,13] Therefore, development of organic semiconductor gain materials, which not only exhibit high carrier mobility and photoluminescence (PL) quantum yield (φ) simultaneously but also possess optimized energy levels that can help decrease bmEA process, is of crucial importance.

Perylenediimide (PDI) derivatives are one of the superstar organic semiconductors widely used in organic thin-film transistors (OTFTs)[14] and photovoltaic solar cells,[15] due to their excellent thermal- and/or photostability, strong electron-

Received: July 4, 2015
Published: November 18, 2015

DOI: 10.1021/jacs.5b10353
J. Am. Chem. Soc. 2015, 137, 15105−15111

accepting character, and their chemically tunable structures via modification at either imide or bay positions.[16] For instance, electron mobility as high as 4.65 $cm^2 V^{-1} s^{-1}$ was reported in n-channel OFETs of tetrachlorinated diperylenebisimide.[17] Moreover, power conversion efficiency > 6.0% was achieved in a solution-processed nonfullerene solar cell using a helical PDI dimer as the electron acceptor.[18] Note that PDI monomers in the dilute solution are highly emissive with $\varphi_{monomer}$ close to 100%, enabling applications such as dye laser, optical sensing, and single molecule spectroscopy.[19] Nonetheless, strong $\pi-\pi$ intermolecular interactions drive PDI molecules form cofacially stacked H-aggregates in the solid state, which exhibit unfavorable, strongly quenched PL properties with φ_H < 1%.[16] This, plus the formation of excimer trap-states in thin film,[20] limits the application of PDIs in light-emitting devices. Although DFB lasers have been demonstrated by doping PDIs into an optically (also electrically) inert polystyrene (PS) film, the concentration of PDIs was typically kept low at 0.5−1 wt % of PDI with respect to PS in order to avoid the concentration quenching effect.[21] To the best of our knowledge, OSSLs based on neat PDIs have not been achieved yet. Here, we demonstrated the first PDI-based OSSL from hexagonal microdisk (hMD) WGM microcavity of *N,N′*-bis(1-ethylpropyl)-2,5,8,11-tetrakis(*p*-methyl-phenyl)-perylenediimide (*mp*-PDI) self-assembled from solution. Single-crystal X-ray diffraction (XRD) analysis revealed that steric hindrance of methylphenyl groups substituted at head-positions drives *mp*-PDI molecules stacking in a loosely packed twisted brickwork arrangement of J-type aggregates, with a solid-state PL efficiency of φ > 15%. This, plus the optical feedback provided by the hMD-WGM microcavity, enables the observation of multimode lasing as evidenced by nonlinear output, spectral narrowing, and temporal coherence of laser emission. More importantly, we found that ultrafast radiative decay due to exciton-vibration coupling in J-aggregates significantly reduces the exciton diffusion length (L_D) and therefore suppresses the bmEA process. These features, such as the moderate optical gain and the absence of bmEA, combine with the high carrier-mobility associated with PDIs, making *mp*-PDI attractive candidates on the way to achieve electrically driven OSSL.

RESULTS AND DISCUSSION

We have synthesized *mp*-PDI via a Ru-catalyzed 4-fold arylation reaction (Scheme 1).[22] A mixture of phenyl boronic acid neopentyl glycol ester and bis(*N*-ethylpropyl)-perylenediimidee (PDI-1) was heated in refluxing mesitylene and pinacolone at 140 °C for 48 h in the presence of 25 mol % [$RuH_2(CO)(PPh_3)_3$] (see the Supporting Information for details). After silica-gel separation, *mp*-PDI was obtained in 59% yield and was characterized by ^{1}H NMR and MALDI-MS (see the Supporting Information).

Scheme 1. Ru-Catalyzed 4-Fold Arylation of *mp*-PDI

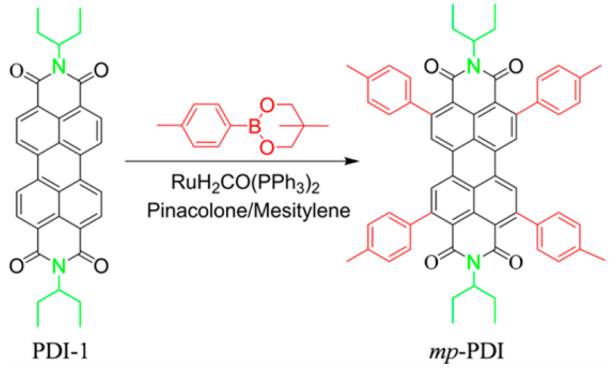

In our experiment, single-crystalline hMDs of *mp*-PDI were prepared via the reprecipitation method,[23] by injection of 100 μL of a stock solution (0.5 mg/mL) in dichloromethane into 0.5 mL of hexane. Within 1 h, hMDs of *mp*-PDI were formed and then centrifugally separated from the suspension and washed twice using hexane prior to vacuum drying.

Figure 1a shows a scanning electron microscopy (SEM) image of typical products deposited on a silicon wafer. It can be seen that hMDs of *mp*-PDI were successfully prepared, which exhibit smooth outer surfaces and sharp edges (also see Figure S1a). The edge-length (W) of hMDs is found to range between 1 and 10 μm, with 80% of MDs having edge-lengths between 3 and 8 μm (Figure S1b). The thickness (T) of hMDs of *mp*-PDI is about 600 nm as shown by a vertically grown hMD in the upper-left of Figure 1a, and is further confirmed by atomic force microscopy (AFM) measurements (Figure S2). Figure 1c depicts a transmission electron microscopy (TEM) image of a single hMD. Selected area electron diffraction (SAED) pattern was recorded by directing the electron beam perpendicular to the flat surface of the single hMD (Figure 1d). The clearly observed rectangular symmetry of SAED spots in Figure 1d clarifies that hMDs of *mp*-PDI are single crystalline in nature.

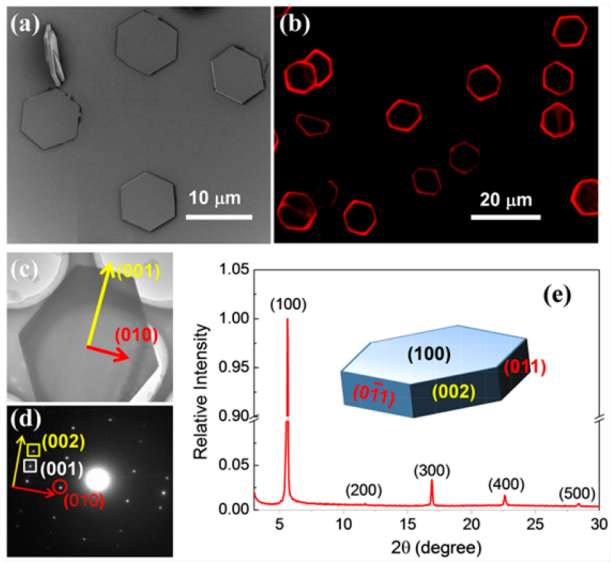

Figure 1. (a) SEM and (b) PL microscopy images of as-prepared hMDs of *mp*-PDI. (d) SAED pattern recorded by directing the electron beam perpendicular to the top-surface of a single hMD shown in (c). (e) XRD spectrum of a mat of hMDs deposited on a silicon wafer. The inset illustrates a cartoon of hMD.

In order to understand the solid-state molecular packing, we also cultivated bulk-crystals suitable for single-crystal X-ray diffraction (XRD) analysis using a solvent diffusion method at the liquid−liquid interface between CH_2Cl_2 and hexane. Monoclinic *mp*-PDI crystals belong to the space group of $C2/c$ with cell parameters of a = 38.429(16) Å, b = 8.548(3) Å, c = 17.774(8) Å, $\alpha = \gamma = 90°$, and β = 112.242(6)° (CCDC No. 1407196, Figure S3a). Based on single-crystal cell parameters, the red circled set of SAED spots in Figure 1d is ascribed to (010) Bragg reflections with $d_{(010)}$ = 8.5 Å, while the white and

DOI: 10.1021/jacs.5b10353
J. Am. Chem. Soc. 2015, 137, 15105−15111

yellow squared sets of SAED spots are ascribed to (001) and (002) Bragg reflections with $d_{(001)}$ = 17.8 Å and $d_{(002)}$ = 8.9 Å, respectively. Figure 1e presents the XRD spectrum of a mat of hMDs deposited on a silicon substrate, which is dominated by a series of peaks corresponding to the crystal plane (100), such as (200), (300), (400), and (500) peaks. This suggests that hMDs of *mp*-PDI adopt a lamellar structure with the crystal (100) plane parallel to the substrate (Figure S3a). Combining SAED and XRD results together, we drew a schematic cartoon of *mp*-PDI hMDs (see the inset of Figure 1e), which are single crystals bound by (100) and (−100) crystal planes on the top and bottom faces and by (002), (00−2), (011), (0−11), (01−1), and (0−1−1) crystal planes on the six side-faces (also see Figure S3b).

It should be pointed out that, different from bay-substituted PDIs, which generally exhibit a highly twisted perylene backbone, head-substituted *mp*-PDI molecule maintains the planarity of the perylene core with four carbonyl oxygen atoms sticking out the perylene plane up and/or down (Figure 2a and b). Figure 2c depicts the packing arrangement of *mp*-PDI molecules within the crystal *bc* plane [that is, the (100) crystal plane], viewed perpendicular to the top-surface of hMDs. It can be seen that *mp*-PDI molecules are packed in a brickwork arrangement,[24] similar to the cases of parent PDI-NH and bay-substituted tetrachloro- and octachloro-PDIs.[25] Specifically, each *mp*-PDI molecule labeled **1** is intercalated between four molecules labeled **2** and vice versa, through molecular contacts between carbonyl oxygen and perylene bay-position carbon atoms, such as C(1)···O′(3), O(1)···C′(7), C(7)···O′(1), and O(3)···C′(1) contacts (3.12 Å, see pink dashed lines in Figure 2c). Because *mp*-PDI molecules **1** and **2** form a dihedral angle about 19.8°, an average $\pi-\pi$ distance of $d_{\pi-\pi}$ = 4.27 Å is obtained as indicated by blue double-arrows between (040) and (0−40) crystal planes in Figure 2c, which is much larger than 3.34 Å reported for parent PDI-NH and 3.40−3.45 Å reported for bay-substituted tetrachloro- and octachloro-PDIs PDIs.[25,26] Therefore, our *mp*-PDI molecules in single-crystalline hMDs arrange in a loosely packed twisted brickstone structure. Furthermore, it can be seen from Figure 2d that orthogonal projections of *mp*-PDI molecules **1** and **2** on the crystal *ac* plane are oriented exactly in the same direction, with their N−N axis tilted at an angle of 42.12° with respect to the crystal *c*-axis. The longitudinal (along the molecular long-axis) and transverse (along the molecular short-axis) displacements between *mp*-PDI **1** and **2** are measured to be d_{L-L} = 5.88 Å (Figure 2d and S4a) and d_{S-S} = 6.17 Å (Figure 2d and S4b), respectively.[27] Therefore, $\pi-\pi$ overlap between each *mp*-PDI molecule and its four neighbors is negligible in the loosely packed twisted brickstone structure (Figure 2d). This is in sharp contrast with most PDI derivatives reported in literature, which generally exhibit strong $\pi-\pi$ overlap owing to small values of $d_{\pi-\pi}$, d_{L-L}, and d_{S-S}.[14−18]

Figure 3a presents the steady-state absorption (solid) and PL (dash dot) spectra of a mat of *mp*-PDI hMDs (red) deposited on a quartz plate and *mp*-PDI monomers (black) in the dilute solution. Table 1 summarizes the related photophysical

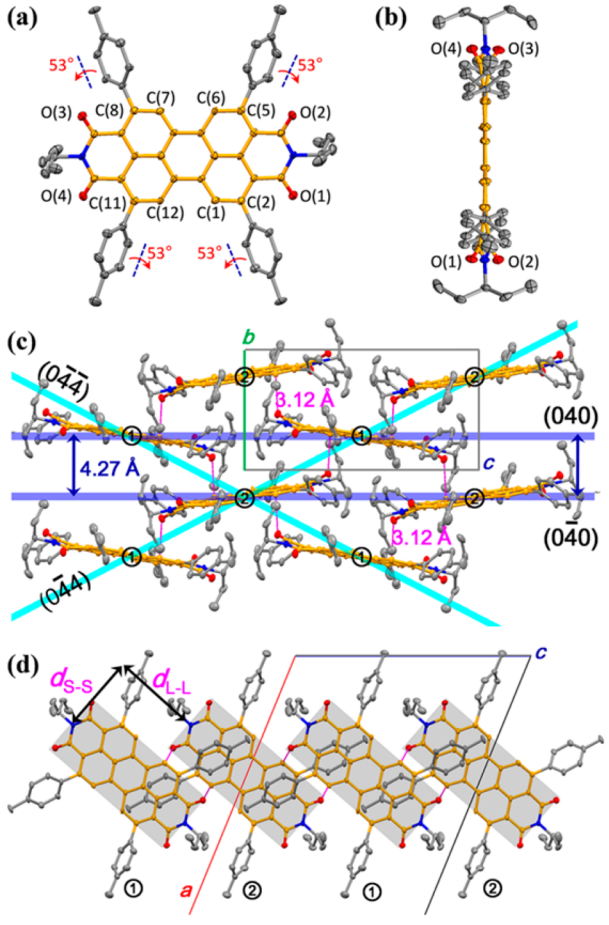

Figure 2. Molecular structures of *mp*-PDI obtained from single-crystal X-ray analysis, viewed perpendicular (a) and parallel (b) to the perylene backbone. Packing arrangements of *mp*-PDI molecules within the crystal *bc* plane (c) and *ac* plane (d). See text for details.

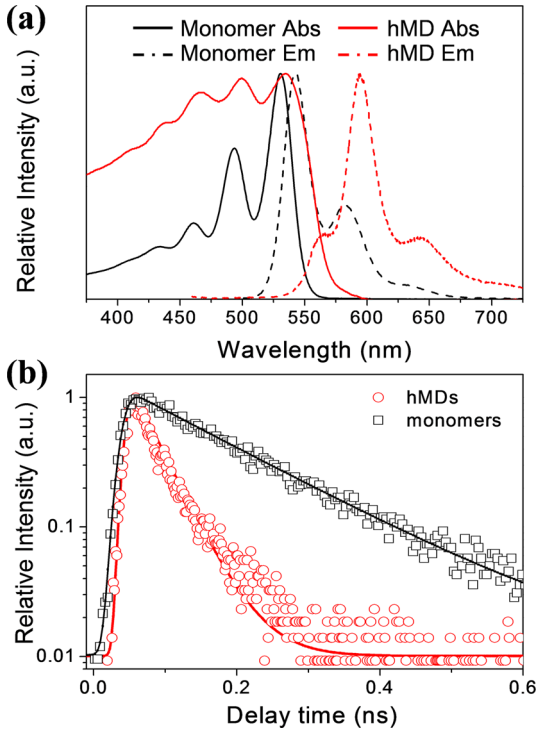

Figure 3. (a) Normalized UV/vis absorption spectra (solid) and PL (dash dot) spectra of a mat of *mp*-PDI hMDs (red) deposited on a quartz plate and *mp*-PDI monomers (black) in the dilute solution. (b) PL decay and fitted curves of *mp*-PDI monomeric solution in CH2Cl2 and hMDs on quartz plate.

DOI: 10.1021/jacs.5b10353
J. Am. Chem. Soc. 2015, 137, 15105−15111

Table 1. Photophysical Parameters of *mp*-PDI Monomers in the Dilute Solution and Solid-State hMDs

sample	λ_{abs} (nm)	λ_{em} (nm)	φ	τ (ns)	k_r (10^8 s^{-1})
monomer	460, 493, 530	542, 584, 635	0.03	0.15	2.0
hMDs	464, 497, 533	560, 595, 645	0.15	0.05	30.0

parameters. The lowest $S_0 \rightarrow S_1$ transition of *mp*-PDI monomers in the dilute solution exhibits a vibronic progression with a subband spacing around 1400 cm^{-1}, while the PL spectrum of monomers shows a mirror structure of its absorption with 0−0, 0−1, and 0−2 emissions at 542, 584, and 635 nm, respectively. The absorption and PL maxima of *mp*-PDI monomers in CH2Cl2 are factually similar to those of monomers of parent PDI-NH (ref 25a) and unsubstituted PDI-1 in the dilute solution (Figure S5a). This suggests that the methylphenyl groups do not conjugate with the perylene backbone in *mp*-PDI, in good agreement with single-crystal structure data, which reveal a dihedral angle of 53° between methylphenyl groups and perylene core (Figure 2a). Notably, we found that the diffused reflectance absorption spectrum of *mp*-PDI hMDs resembles that of monomers (Figure 3a). And the 0−0, 0−1, and 0−2 emission bands of *mp*-PDI hMDs at 560, 595, and 645 nm, respectively, are only slightly red-shifted as compared with those of monomers (Table 1). The similarity between spectral features of *mp*-PDI monomers and hMDs suggest weak intermolecular interactions in the solid state, as evidenced by large $\pi-\pi$ distance of $d_{\pi-\pi}$ = 4.27 Å (Figure 2c) and negligible $\pi-\pi$ overlap between *mp*-PDI molecules (Figure 2d). Recently, Wasielewski and co-workers reported a molecule, namely, *p*-PDI, which is also head-substituted but by phenyl groups (methylphenyl groups in our *mp*-PDI) and presents *n*-octyl chains at imide nitrogen positions (ethylpropyl groups in our *mp*-PDI).[28] Single crystal data reveal that head-substituted *p*-PDI molecules form face-to-face slip-stacked columns with $d_{\pi-\pi}$ = 3.40 Å, d_{L-L} = 3.29 Å, and d_{S-S} = 0.28 Å. As a result, the strong $\pi-\pi$ stacking makes the absorption and PL spectra of *p*-PDI aggregates significantly red-shifted than those of *p*-PDI monomers.[28]

As mentioned above, most PDI derivatives are highly fluorescent in the dilute solution, but are poorly emissive in the solid-state owing to the formation of H-aggregates and excimer traps. By measuring the PL quantum yield (φ) through a relative method for the monomer solution in CH2Cl2 by using Rhodamine 6G as a standard and through an absolute method for hMDs by using an integration sphere, however, we found that *mp*-pDI monomers are poorly emissive in the dilute solution ($\varphi_{m,mp\text{-PDI}}$ = 0.03 ± 0.01), but hMDs exhibit a moderate value of $\varphi_{hMD,mp\text{-PDI}}$ = 0.15 ± 0.02 (Table 1).

To obtain further information on the nature of the excited states, we also measured the PL lifetimes by using a streak camera (Figure 3b). The monomer emission at 542 nm decays monoexponentially, yielding a lifetime of $\tau_{m,mp\text{-PDI}}$ = 0.15 ± 0.02 ns (black line in Figure 3b). The PL decay of hMDs at 595 nm was also fitted monoexponentially with a time constant of $\tau_{hMD,mp\text{-PDI}}$ = 0.05 ± 0.01 ns (red line in Figure 3b). According to the equation, $k = \varphi/\tau$,[25] the radiative decay rates (k) are calculated to be $k_{m,mp\text{-PDI}} = 2.0 \times 10^8$ s^{-1} and $k_{hMD,mp\text{-PDI}} = 30.0 \times 10^8$ s^{-1} for *mp*-PDI monomers and hMDs, respectively (Table 1). (i) Although *mp*-PDI monomers are poorly emissive in the dilute solution, the value of $k_{m,mp\text{-PDI}} = 2.0 \times 10^8$ s^{-1} is factually comparable to those of parent PDI-NH,[25a] unsubstituted PDI-1 (Table S1), and bay-substituted PDIs.[25b] Therefore, the low value of $\varphi_{m,mp\text{-PDI}}$ = 0.03 ± 0.01 is probably a result of fast nonradiative decay caused by rotational motion of methylphenyl substituents in *mp*-PDI (see Figure 2a and b).[29] (ii) $k_{hMD,mp\text{-PDI}}$ is about 15 times higher than k_m. Such enhanced radiative decay (known as "superradiance") is a key characteristic of J-aggregates, attributed to exciton delocalization as a result of the coupling of the transition dipole moments of aggregated chromophores.[24] Moreover, the fact of $k_{hMD,mp\text{-PDI}} > k_{m,mp\text{-PDI}}$ excludes the formation of excimer trap-states, probably a result of the large $\pi-\pi$ distance of $d_{\pi-\pi}$ = 4.27 Å in *mp*-PDI hMDs.[20] It is well-known that the transition dipole of PDIs is along the N−N axis.[16c] Returning to Figure 2c, within (0−44) [or (0−4−4)] crystal plane, the angle between the transition dipole and the packing direction is 42.2° and 53.4° for *mp*-PDI molecule **1** (or **2**) and **2** (or **1**) (also see Figure S4), respectively, placing the alignment in J-aggregate regime but close to the magic angle of 54.7°.[24a] For a typical J-aggregate, one would expect the electronic origin (0−0 transition) to carry the highest oscillator strength.[24b] However, the PL spectrum of *mp*-PDI hMDs in Figure 3a exhibits a 0−1 emission peak stronger than the 0−0 emission peak. This is due to self-absorption effect as a result of small Stokes shift typical for J-aggregate (Figure S6a). Furthermore, the 0−0 emission peak of *mp*-PDI hMDs is found to be enhanced at 77 K as compared with that at room temperature (Figure S6c), consistent with the J-aggregation model developed by Spano.[24b] According to the equation $N = k_{hMD}/k_m$, the size of the coherent domain can be estimated to be $N \approx 15$ molecules in J-aggregation hMDs of *mp*-PDI.[30] In sharp contrast, in the case of unsubstituted PDI-1 (Table S1), the radiative decay rate of weakly emissive H-aggregates, $k_{H,PDI\text{-}1} = 0.77 \times 10^8$ s^{-1} ($\varphi_{H,PDI\text{-}1}$ = 0.05 ± 0.01, $\tau_{H,PDI\text{-}1}$ = 0.65 ± 0.15 ns), is slower than that of highly emissive monomers in the dilute solution, $k_{m,PDI\text{-}1} = 1.7 \times 10^8$ s^{-1} ($\varphi_{m,PDI\text{-}1}$ = 0.95 ± 0.01, $\tau_{hMD,PDI\text{-}1}$ = 5.55 ± 0.15 ns).[24b]

To further explore the PL properties of an individual hMD, we used a homemade optical microscope equipped with a 50× 0.9 NA objective (Figure S7). The second harmonic of a 1 kHz Ti:sapphire regenerative amplifier (λ = 400 nm, pulse width 150 fs) is focused to a 20 μm diameter spot to excite the isolated single hMD placed on a 2D movable table. Spatially resolved PL spectra with a resolution about 1 μm are then collected underneath by using a three-dimensional movable objective coupled to an optical fiber and detected using a liquid-nitrogen cooled charge-coupled device (CCD).

Figure 4a shows the PL spectra of an isolated hMD (W = 5.5 μm) with increasing the pump intensity of 400 nm laser (P). At P = 1.65 $\mu J/cm^2$, the PL spectrum of *mp*-PDI hMD is presented as a broad spontaneous emission. When the pump density reaches a threshold from P = 11.8 to 14.6 $\mu J/cm^2$, strong laser emission arises as a set of sharp peaks on the top of the 0−1 transition. This agrees with the fact that the 0−1 transition has the maximum net gain in four-level organic laser system,[1a] because unoccupied vibronic sublevels of the ground state in thermal equilibrium facilitates the buildup of population inversion.[2] Figure 4b shows the integrated intensities of the 0−1 peak as a function of P, which demonstrates a threshold at P_{th} = 10.8 $\mu J/cm^2$. The intensity dependence is fitted to a

DOI: 10.1021/jacs.5b10353
J. Am. Chem. Soc. 2015, 137, 15105−15111

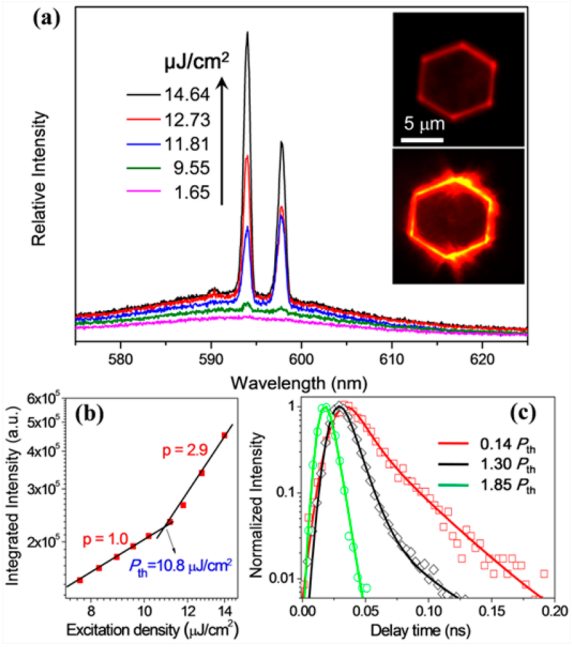

Figure 4. (a) μ-PL spectra of a single hMD with W = 5.5 μm under different pump pulse densities at room temperature. (b) Integrated area of the 0−1 peak as a function of pump density. The lasing threshold is identified as the intersection between the linear and superlinear regions. (c) PL decay profiles of hMD monitored at 595 nm, showing the evolution from unquenched spontaneous emission to lasing emission, with increasing the pumping laser power. Above the threshold, the decay time always collapses to <10 ps, indicating an effective stimulated process. The bmEA is nearly disappears below the threshold so that the decay time changes little.

power law x^p (ref 2), with p = 1.04 ± 0.05 and 2.93 ± 0.11 below and above the threshold, respectively. The latter p = 2.93 ± 0.11 above the threshold indicates a superlinear increase of PL output, characteristic of laser emission. In previous studies,[2,5−8,23] however, $p \approx 0.5$ has been exclusively reported below the threshold owing to the presence of bmEA process. Therefore, p = 1.04 ± 0.05 obtained for *mp*-PDI hMD below the threshold suggests the absence of bmEA.

To gain further insight, we investigated the PL lifetimes at different pump intensities. As mentioned above, PL of individual hMD follows single exponential decay with $\tau_{\text{hMD},mp\text{-PDI}}$ = 0.05 ± 0.01 ns at a very low excitation density of $P = 0.01P_{\text{th}}$. Upon increasing the pump intensity to $P = 0.14P_{\text{th}}$ and/or $0.8P_{\text{th}}$, the PL decay changes little. This further confirms the absence of bimolecular quenching. Note that bmEA process is related to collision of excitons, controlled by the exciton diffusion according to $L_D = (\tau D)^{1/2}$, where D is the diffusion coefficient, and τ and L_D the exciton lifetime and diffusion length, respectively.[31] Using $D = 5 \times 10^{-4}$ cm^2 s^{-1} and $\tau = 10^{-9}$ s (typical for organic semiconductors),[31] L_D = 7.1 nm is obtained. In our case, $\tau_{\text{hMD},mp\text{-PDI}}$ = 0.05 ± 0.01 ns gives rise to L_D = 1.6 nm, just equal to the size of a single *mp*-PDI molecule. That is, the fast radiative decay of *mp*-PDI J-aggregate significantly decreases the exciton diffusion length, thereby avoiding the exciton collision, i.e., the bmEA process. In sharp contrast, the fluorescence intensity dependence of PDI-1 H-aggregation film is fitted to a power law x^p with p = 0.46 ± 0.05 (Figure S8), indicating the occurrence of bmEA even at low excitation density.[2,7b] Previously, femtosecond transient absorption (fsTA) measurement on conjugated polymer thin-film identified extremely short-lived gain through monitoring the stimulated emission process (ref 1a and references therein). By performing fsTA on 100 nm thick thin-films (Figure S9), stimulated emission signal is clearly observed for *mp*-PDI film, but is undetectable for PDI-1 film. Therefore, the absence of bmEA process can greatly help the buildup of optical gain in J-aggregation hMDs of *mp*-PDI. In any event, it can be seen from Figure 4c that above the threshold, for instance, at $P = 1.3P_{\text{th}}$ and $1.8P_{\text{th}}$, the PL decay time of *mp*-PDI hMD collapses to <10 ps, demonstrating an effective stimulated process within the hMD microcavity.

Returning to Figure 4a, the upper and lower insets show the μ-PL images of the 5.5 μm width hMD below and above the lasing threshold, respectively. And six bright edges are observed due to light leakage. This suggests that six side-faces of *mp*-PDI hMDs form a WGM microresonator. Note that semiconductor microdisk WGM resonators, in which photons are strongly confined through successive total internal reflection along the disk circumference, have been widely used for acquiring narrow-line width and low-threshold microlasers.[7a] Recently, well-faceted WGM microlasers based on self-assembled single-crystalline organic microdisks have been also demonstrated.[7b] The inset of Figure 5b presents a classical optical ray analysis

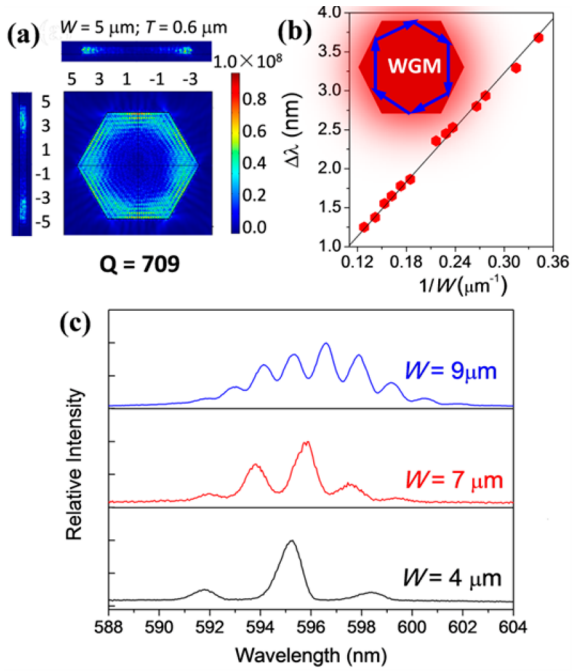

Figure 5. (a) Optical mode simulation results for an hMD with W = 5 μm and T = 0.6 μm. (b) Mode spacing $\Delta\lambda$ at λ = 596 nm versus $1/W$ of hMDs, showing clearly a linear relationship. Inset illustrates a typical optical-ray analysis within WGM-hMD microcavity. (c) High-resolution PL spectra of laser emission recorded above threshold for hMDs with W = 9, 7, and 4 μm.

within WGM-hMD microcavity of *mp*-PDI. It is well-known that total internal reflection (TIR) takes place at the hMD/air interfaces if $\psi \geq \arcsin(1/n_r)$, where ψ is the angle of incidence light with respect to the normal of the given facet and n_r is relative phase refraction index.[7b] With $n_{r,\text{PDI}}$ = 1.8 for *mp*-PDI, the smallest angle of TIR is ψ_{TIR} = 33.7°. As shown in the inset of Figure 5b, ψ = 60° for 6-WGM is larger than ψ_{TIR} = 33.7°, suggesting that our hMDs can indeed support 6-WGM microcavities.

DOI: 10.1021/jacs.5b10353
J. Am. Chem. Soc. 2015, 137, 15105−15111

To further understand the lasing modes in *mp*-PDI hMDs, we performed optical mode simulation for an hMD (5 μm in width and 600 nm in thickness) placed on a quartz plate by using the finite-difference time-domain (FDTD) method with parameters of refractive indexes of *mp*-PDI ($n_{r,PDI}$ = 1.8) and quartz (n_{quartz} = 1.4). Figure 5a shows the absolute electric field distribution $|E|^2$ patterns of a TM-mode, viewed perpendicular to the hexagonal top-surface. As one can see, this TM-mode is well-confined in the hMD and reflected between the six side-faces. The cavity quality factor (Q) is calculated to be 709 for this TM-mode. We also measured the Q experimentally according to $Q = \lambda/\delta\lambda$, where λ and $\delta\lambda$ are the wavelength and full-width at half-maximum of the lasing peak, respectively.[7b,23] And λ = 595 nm and $\delta\lambda$ = 1.05 nm from Figure 4a gives rise to Q = 567, which is comparable to the theoretical value.

In order to understand the effect of the hMD size on the cavity effect, we investigated a series of hMDs with W = 4, 7, and 9 μm. It can be seen from Figure 5c that the lasing spectra of hMDs exhibit more and more modes with increasing the hMD side-length. Therefore, the spacing between adjacent modes, $\Delta\lambda$, decreases with increasing the value of W, for instance, $\Delta\lambda$ = 3.64, 1.78, and 1.25 nm for W = 4, 7, and 9 μm, respectively (Figure 5c). It is known that $\Delta\lambda$ at wavelength λ for a WGM cavity with a cavity length of L is given by $\Delta\lambda = \lambda^2/L[n - \lambda(dn/d\lambda)]$, where $[n - \lambda(dn/d\lambda)]$ is the group refractive index.[7b,23] According to geometric conditions, $L = 3\sqrt{3}W$ is obtained for an hMD-WGM microcavity of *mp*-PDI. Figure 5b plots the value of $\Delta\lambda$ at λ = 595 nm as a function of $1/W$, demonstrating clearly a linear relationship. This further confirms the built-in WGM microcavity within *mp*-PDI hMDs. Moreover, we found that the Q value increases with increasing the cavity length Q = 163, 334, and 476 for W = 4, 7, and 9 μm, respectively, in good agreement with optical simulation results (Figure S10).

CONCLUSION

In conclusion, we demonstrated the first PDI-based OSSL from WGM-hMD microcavity of *mp*-PDI self-assembled from solution. Single-crystal results reveal that *mp*-PDI molecules stack in a loosely packed twisted brickwork arrangement of J-type aggregates in hMDs, which exhibit a solid-state PL efficiency of φ > 15%. More importantly, we found that exceptional fast radiative decay due to exciton-vibration coupling in J-aggregates significantly reduces the exciton diffusion length (L_D) and therefore avoids the bmEA process. These features, such as the moderate opdatical gain and the absence of bmEA, plus the optical feedback provided by WGM-hMD microcavity, enable the observation of multimode lasing. With consideration of high carrier-mobility associated with PDIs, hMDs of *mp*-PDI are attractive candidates on the way to achieve electrically driven OSSL.

ASSOCIATED CONTENT

Supporting Information

The Supporting Information is available free of charge on the ACS Publications website at DOI: 10.1021/jacs.5b10353.

General synthesis procedures, spectral data, and optical simulation results (PDF)

CIF file for the X-ray analysis of *mp*-PDI single-crystal with CCDC No. 1407196 (CIF)

AUTHOR INFORMATION

Corresponding Authors

*hongbing.fu@iccas.ac.cn

*yswu@iccas.ac.cn

Notes

The authors declare no competing financial interest.

ACKNOWLEDGMENTS

This work was supported by the National Natural Science Foundation of China (Nos. 91222203, 21273251, 91333111, 21190034, 21221002), project of State Key Laboratory on Integrated Optoelectronics of Jilin University (IOSKL2014KF16), project of Construction of Innovative Teams and Teacher Career Development for Universities and Colleges Under Beijing Municipality (IDHT20140512), the National Basic Research Program of China (973) 2011CB808402, 2013CB933500, and the Chinese Academy of Sciences.

REFERENCES

(1) (a) Turnbull, I. D. *Chem. Rev.* **2007**, *107*, 1272−1295. (b) Service, R. F. *Science* **2010**, *328*, 810−811.

(2) Kena Cohen, S.; Forrest, S. R. *Nat. Photonics* **2010**, *4*, 371−375.

(3) Berggren, M.; Dodabalapur, A.; Slusher, R. E.; Timko, A.; Nalamasu, O. *Appl. Phys. Lett.* **1998**, *72*, 410.

(4) Wang, H.; Li, F.; Gao, B.; Xie, Z.; Liu, S.; Wang, C.; Hu, D.; Shen, F.; Xu, Y.; Shang, H.; Chen, Q.; Ma, Y.; Sun, H. *Cryst. Growth Des.* **2009**, *9*, 4945−4950.

(5) Kozlov, V. G.; Bulovic, V.; Burrows, P. E.; Forrest, S. R. *Nature* **1997**, *389*, 362−364.

(6) Wallikewitz, B. H.; de la Rosa, M.; Kremer, J. H.; Hertel, D.; Meerholz, K. *Adv. Mater.* **2010**, *22*, 531−534.

(7) (a) He, L.; Özdemir, S. K.; Yang, L. *Laser Photonics Rev.* **2013**, *7*, 60−81. (b) Wang, X. D.; Liao, Q.; Kong, Q. H.; Zhang, Y.; Xu, Z. Z.; Lu, X. M.; Fu, H. B. *Angew. Chem., Int. Ed.* **2014**, *53*, 5863−5867.

(8) Hu, X.; Jiang, P.; Ding, C.; Yang, H.; Gong, Q. *Nat. Photonics* **2008**, *2*, 185−189.

(9) (a) Xia, R.; Heliotis, G.; Bradley, D. D. C. *Appl. Phys. Lett.* **2003**, *82*, 3599. (b) Riedl, T.; Rabe, T.; Johannes, H. H.; Kowalsky, W.; Wang, J.; Weimann, T.; Hinze, P.; Nehls, B.; Farrell, T.; Scherf, U. *Appl. Phys. Lett.* **2006**, *88*, 241116.

(10) Xing, G.; Mathews, N.; Lim, S. S.; Yantara, N.; Liu, X.; Sabba, D.; Grätzel, M.; Mhaisalkar, S.; Sum, T. C. *Nat. Mater.* **2014**, *13*, 476−480.

(11) (a) Payne, M. M.; Parkin, S. R.; Anthony, J. E.; Jackson, T. N. *J. Am. Chem. Soc.* **2005**, *127*, 4986−4987. (b) Yang, J.; Yan, D.; Jones, T. S. *Chem. Rev.* **2015**, *115*, 5570−5603. (c) da Silva Filho, D. A.; Kim, E. G.; Brédas, J. L. *Adv. Mater.* **2005**, *17*, 1072−1076.

(12) (a) Chénais, S.; Forget, S. *Polym. Int.* **2012**, *61*, 390−402. (b) Murawski, C.; Leo, K.; Gather, M. C. *Adv. Mater.* **2013**, *25*, 6801−6827.

(13) Komino, T.; Nomura, H.; Koyanagi, T.; Adachi, C. *Chem. Mater.* **2013**, *25*, 3038−3047.

(14) Usta, H.; Facchetti, A.; Marks, T. J. *Acc. Chem. Res.* **2011**, *44*, 501−510.

(15) Hartnett, P. E.; Timalsina, A.; Matte, H. S.; Zhou, N.; Guo, X.; Zhao, W.; Facchetti, A.; Chang, R. P.; Hersam, M. C.; Wasielewski, M. R.; Marks, T. J. *J. Am. Chem. Soc.* **2014**, *136*, 16345−16356.

(16) (a) Figueira-Duarte, T. M.; Mullen, K. *Chem. Rev.* **2011**, *111*, 7260−7314. (b) Huang, C.; Barlow, S.; Marder, S. R. *J. Org. Chem.* **2011**, *76*, 2386−2407. (c) Wurthner, F. *Chem. Commun.* **2004**, 1564−1579.

(17) Lv, A.; Puniredd, S. R.; Zhang, J.; Li, Z.; Zhu, H.; Jiang, W.; Dong, H. L.; He, Y.; Jiang, L.; Li, Y.; Pisula, W.; Meng, Q.; Hu, W. P.; Wang, Z. H. *Adv. Mater.* **2012**, *24*, 2626−2630.

DOI: 10.1021/jacs.5b10353
J. Am. Chem. Soc. 2015, 137, 15105−15111

(18) Zhong, Y.; Trinh, M. T.; Chen, R. S.; Wang, W.; Khlyabich, P. P.; Kumar, B.; Xu, Q. Z.; Nam, C.-Y.; Sfeir, M. Y.; Black, C.; Steigerwald, M. L.; Loo, Y.-L.; Xiao, S. X.; Ng, F.; Zhu, X.-Y.; Nuckolls, C. *J. Am. Chem. Soc.* **2014**, *136*, 15215−15221.
(19) (a) Calzado, E. M.; Villalvilla, J. M.; Boj, P. G.; Quintana, J. A.; Gomez, R.; Segura, J. L.; Diaz-Garcia, M. A. *J. Phys. Chem. C* **2007**, *111*, 13595−13605. (b) Siekierzycka, J. R.; Hippius, C.; Wurthner, F.; Williams, R. M.; Brouwer, A. M. *J. Am. Chem. Soc.* **2010**, *132*, 1240−1242. (c) Weil, T.; Vosch, T.; Hofkens, J.; Peneva, K.; Mullen, K. *Angew. Chem., Int. Ed.* **2010**, *49*, 9068−9093.
(20) Fink, R. F.; Seibt, J.; Engel, V.; Renz, M.; Kaupp, M.; Lochbrunner, S.; Zhao, H. M.; Pfister, J.; Wurthner, F.; Engels, B. *J. Am. Chem. Soc.* **2008**, *130*, 12858−12859.
(21) (a) Ramirez, M. G.; Pla, S.; Boj, P. G.; Villalvilla, J. M.; Quintana, J. A.; Diaz-Garcia, M. A.; Fernandez-Lazaro, F.; Sastre-Santos, A. *Adv. Opt. Mater.* **2013**, *1*, 933−938. (b) Ramirez, M. G.; Morales-Vidal, M.; Navarro-Fuster, V.; Boj, P. G.; Quintana, J. A.; Villalvilla, J. M.; Retolaza, A.; Merino, S.; Diaz-Garcia, M. A. *J. Mater. Chem. C* **2013**, *1*, 1182−1191.
(22) (a) Nakazono, S.; Easwaramoorthi, S.; Kim, D.; Shinokubo, H.; Osuka, A. *Org. Lett.* **2009**, *11*, 5426−5429. (b) Battagliarin, G.; Zhao, Y.; Li, C.; Müllen, K. *Org. Lett.* **2011**, *13*, 3399−3401.
(23) Wang, X. D.; Liao, Q.; Lu, X. M.; Li, H.; Xu, Z. Z.; Fu, H. B. *Sci. Rep.* **2014**, *4*, 7011.
(24) (a) Wurthner, F.; Kaiser, T. E.; Saha-Moller, C. R. *Angew. Chem., Int. Ed.* **2011**, *50*, 3376−3410. (b) Spano, F. C. *Acc. Chem. Res.* **2010**, *43*, 429−439.
(25) (a) Cao, X. Q.; Wu, Y. S.; Fu, H. B.; Yao, J. N. *J. Phys. Chem. Lett.* **2011**, *2*, 2163−2167. (b) Cao, X. Q.; Bai, S. M.; Wu, Y. S.; Liao, Q.; Shi, Q.; Fu, H. B.; Yao, J. N. *Chem. Commun.* **2012**, *48*, 6402−6404. (c) Gsanger, M.; Oh, J. H.; Konemann, M.; Hoffken, H. W.; Krause, A. M.; Bao, Z. N.; Wurthner, F. *Angew. Chem., Int. Ed.* **2010**, *49*, 740−743.
(26) (a) Klebe, G.; Graser, F.; Hadicke, E.; Berndt, J. *Acta Crystallogr., Sect. B: Struct. Sci.* **1989**, *45*, 69−77. (b) Kaiser, T. E.; Stepanenko, V.; Wurthner, F. *J. Am. Chem. Soc.* **2009**, *131*, 6719−6732.
(27) Curtis, M. D.; Cao, J.; Kampf, J. W. *J. Am. Chem. Soc.* **2004**, *126*, 4318−4328.
(28) Eaton, S. W.; Shoer, L. E.; Karlen, S. D.; Dyar, S. M.; Margulies, E. A.; Veldkamp, B. S.; Ramanan, C.; Hartzler, D. A.; Savikhin, S.; Marks, T. J.; Wasielewski, M. R. *J. Am. Chem. Soc.* **2013**, *135*, 14701−14712.
(29) Hong, Y.; Lam, J. W.; Tang, B. Z. *Chem. Commun.* **2009**, *29*, 4332−4353.
(30) Kaiser, T. E.; Wang, H.; Stepanenko, V.; Wurthner, F. *Angew. Chem., Int. Ed.* **2007**, *46*, 5541−5544.
(31) Shaw, P. E.; Ruseckas, A.; Samuel, I. D. W. *Adv. Mater.* **2008**, *20*, 3516−3520.

DOI: 10.1021/jacs.5b10353
J. Am. Chem. Soc. 2015, 137, 15105−15111